JOURNAL OF PROPULSION AND POWER
Vol. 27, No. 2, March–April 2011

Dynamic Response of Rocket Swirl Injectors, Part I: Wave Reflection and Resonance

Maksud Ismailov* and Stephen D. Heister†
Purdue University, West Lafayette, Indiana 47907

DOI: 10.2514/1.B34044

Linear analyses are developed to theoretically investigate how disturbance waves are reflected and transmitted in the vortex chamber of a classical swirl injector. The dependence of the magnitude of the wave reflection process on the disturbance frequency is derived, and it is shown that this dependence may exhibit distinct maximum values. It is explained that the frequencies at which maximum response occurs are termed the resonant frequencies of the swirl injector. In general, resonant conditions will depend not only on the geometry of the injector but also on the particular flow conditions. In other words, for a given injector geometry, there are specific flow conditions that may produce resonance. A simple formula is derived for the primary resonance, which corresponds to a quarter-wave oscillation within the vortex chamber. Two different resonance theories are presented that vary in their level of accuracy of description of the flow transition from the vortex chamber to the nozzle. Results are provided for both of these models.

Nomenclature

C	=	angular momentum constant, $u_\theta r$
f	=	disturbance frequency
k	=	wave number, $\frac{2\pi}{\lambda}$
k_n	=	wave number in uniform nozzle region
L_c	=	length of conical convergence section
L_n	=	length of nozzle
L_v	=	length of vortex chamber
N_{in}	=	number of tangential inlets
R	=	radius of solid boundary
R_{in}	=	inflow radius, $R_v - R_t$
R_n	=	radius of nozzle
R_t	=	radius of tangential inlet
R_v	=	radius of vortex chamber
r_{he}	=	steady free surface radius at head end
r_n	=	steady free surface radius in uniform nozzle region
r_v	=	steady free surface radius in uniform vortex chamber region
u_z	=	axial velocity
u_{zn}	=	axial velocity in uniform nozzle region
u_{zv}	=	axial velocity in uniform vortex chamber region
u_θ	=	circumferential velocity
W_{in}	=	tangential inlet inflow velocity
α	=	angle of solid wall convergence
δ	=	steady free surface radius at any axial position of internal flow
η	=	free surface deflection away from δ
λ	=	wavelength
Π_{inj}	=	total injector response
ω	=	angular disturbance frequency
$()'$	=	fluctuation value of parameter
$\bar{()}$	=	steady-state value of parameter
$\hat{()}$	=	amplitude of fluctuation of disturbed parameter
$()^*$	=	dimensional value of parameter

Received 11 June 2010; revision received 17 September 2010; accepted for publication 3 November 2010.

*Graduate Research Assistant, School of Aeronautics and Astronautics, 701 West Stadium Avenue. Student Member AIAA.

†Professor, School of Aeronautics and Astronautics, 701 West Stadium Avenue. Associate Fellow AIAA.

I. Introduction

SWIRL injectors, or simplex atomizers, are used in a variety of applications ranging from agricultural sprays to use within high-flow aerospace combustors. In particular, these injectors have seen wide application in Russian rocket engines and in numerous gas turbine engines. In these applications, it is well known that the injector can play a role in stabilizing or destabilizing combustion processes, as it acts as an active element within the system; in particular, the injector response at acoustic modes of the chamber is highly critical. Should the injector exhibit a resonance condition at a fundamental chamber acoustic frequency, the potential exists for rapid growth of combustion instabilities. For this reason, the dynamic response of swirl injectors is a topic of significant importance in this community.

Despite this interest, there are rather limited works that discuss the dynamic response of swirl injectors. The most widely recognized analytical work in this field is the 1979 book by Bazarov [1], who developed a linear theory based on small disturbances propagating through the injector flow. Overall, Bazarov's theory [1,2] presents itself as a valuable analytical tool that may predict the expected strength of injector response one can expect. Before Bazarov's work [1], there did not exist any theory similar to this one in its level of extensive description of injector dynamics. Because this is the current standard for use in analysis of dynamic response of swirl injectors, we developed an in-house code to be able to use this as a predictive capability within our group. The code was validated against results published within Bazarov's book [1]. The code was exercised over a range of conditions in order to assess its behavior [3] (Chap. 2). As a result of these efforts, we identified several aspects of the theory that provide motivation for improvements and further study.

Regarding surface wave treatment, we identified the following:

1) The variation of internal flow boundaries is simplified to the case of sudden film thickness change as the vortex chamber transitions to the nozzle, which permits one to ignore wave refraction and results in a reflection coefficient that does not depend on the disturbance frequency.

2) When treating surface waves, which are reflecting back and forth in the vortex chamber, the wave speed taken for both downstream and upstream traveling disturbances is such that it is valid for downstream traveling disturbances only.

3) Only long-wave speed relations are considered, which do not formally apply at high disturbance frequencies, where Thomson's [4] dispersion becomes more appropriate.

Regarding vorticity wave treatment, we identified the following:

1) The process of liquid issuing from the injector tangential inlet into the vortex chamber is represented by a conformal mapping of the

half-strip into the half-plane; however, no clear theoretical evidence exists to justify this representation.

2) To determine the phase shift in the radial direction, the expression for steady-state radial velocity is used that does not obey Laplace's equation describing the potential flow at the steady state.

3) To compute the time lag in the radial direction, the radial distance from the cylindrical wall of the vortex chamber to the point of interest at some arbitrary radius is divided by the steady radial velocity corresponding to this point; however, it is not taken into account that this radial velocity actually varies with radius, so an integral expression for the time lag should be used.

These issues provided motivation for the present study.

More recently, Park [5] investigated the dynamics of swirl injectors by using an axisymmetric boundary element method (BEM) that assumes that the flow is incompressible and irrotational. The way Park modeled the flow unsteadiness was by sinusoidally fluctuating the inflow velocity, while the pressure inside the core remained constant. His work was among the first that attempted to model the unsteady dynamics of swirl injectors by methods of computational fluid dynamics. Richardson [6] and Richardson et al. [7] continued the previously mentioned work of Park [5], relaxed the condition of constant gas pressure in the core, and allowed it to fluctuate. Then, the inflow velocity was computed based on instantaneous pressure drop and the radius of the core surface at the head end. Recently, a research group in Korea [8,9] pulsed the flow in the range of frequencies of 100–300 Hz and presented the experimental data for the pressures and mass flow rates. Experimental results have also been published by Ahn [10] and Ahn et al. [11], whose work is aimed at achieving response data in the broader frequency range, possibly the same as in Bazarov's [1] experiments.

Figure 1 provides a schematic of a classical swirl injector. An air core evolves at the center of the injector due to the vortical inflow. The shape of the free surface, shown schematically in Fig. 1, has a head-end transition region that results from the flow accelerating in the axial direction from its initial tangential injection. A similar transition region exists near the nozzle as the flow is accelerated via the conical convergence section. One of the major hurdles one must undertake to assess the dynamic response of a swirl injector relates to the propagation, refraction, and reflection of waves that form on the free surface of the liquid film. Complex dynamic patterns can result from interaction of these waves and, as the flow is swirling, the undulations can also lead to local changes in the swirl level. For these reasons, the analysis of the dynamic response of these injectors is quite challenging. In this study, we focus on the disturbance wave reflections and the resonance caused by them. There is no indication in the existing literature that this topic has been investigated to date. Note that, at the present time, all analytical models describing the steady-state injector free surface do not consider the head end and the nozzle entrance transition regions at all, because the engineering design interest lies mainly in finding the core radii in the uniform regions of the injector (Taylor [12], Bayvel and Orzechowski [13], and Bazarov [1]). In reality, the variation of the free surface shape in the said transition regions does take place, and it is smooth and continuous, which sets the favorable conditions for the wave refractions and reflections to occur [3], as follows next.

Imagine that an incident wave has been induced in the vortex chamber and is moving in the positive axial direction toward the nozzle. At the entry to the conical convergence section, an abrupt change in the bulk flow velocity and the liquid film thickness takes place. Thus, when an incident wave arrives at that discontinuity plane, one portion of it reflects back into the vortex chamber, in the negative axial direction, and another portion transmits further into the transition region. Now, let us track the reflected portion of it in the vortex chamber. When the reflected wave comes to the head-end solid wall, it is reflected once again, in the positive axial direction. Thus, we see two planes generating a wave reflection, suggesting that a standing wave pattern may be arranged in the vortex chamber.

The amplitude of the resulting standing wave depends on the reflection and transmission characteristics quantifying the events of the reflections just described. Because these characteristics depend on the disturbance frequency, there may be frequencies at which this amplitude is maximized. These frequencies are the natural frequencies of the swirl injector. Since the swirl injector is coupled to the combustion chamber of the rocket engine, a resonance may occur when the combustion instability frequency coincides with one of the natural frequencies of the injector. Accordingly, further on, we will refer to the natural frequencies of the swirl injector as the resonant frequencies. For this reason, it is highly desirable to be able to predict these resonant conditions, and that is the prime motivation for the present study.

We can treat this problem by using three different levels of approximation, depending on what parts of the injector are included in the analysis. In the first approximation, in Sec. IV, we consider the vortex chamber and the nozzle by assuming that they are connected by a sharp (radial) step, and we look for the nozzle effect on the wave reflection and resonance characteristics. We shall refer to this treatment as the abrupt convergence resonance model, or ACRM. In the second approximation, in Sec. V, we consider all three elements of the swirl injector (the vortex chamber, the conical convergent section, and the nozzle) and look for their collective influence on the wave reflection and resonance. We shall refer to this as the conical convergence resonance model, or CCRM.

In both approximations, we approach this problem by matching the instantaneous mass flow rate and momentum fluctuations at

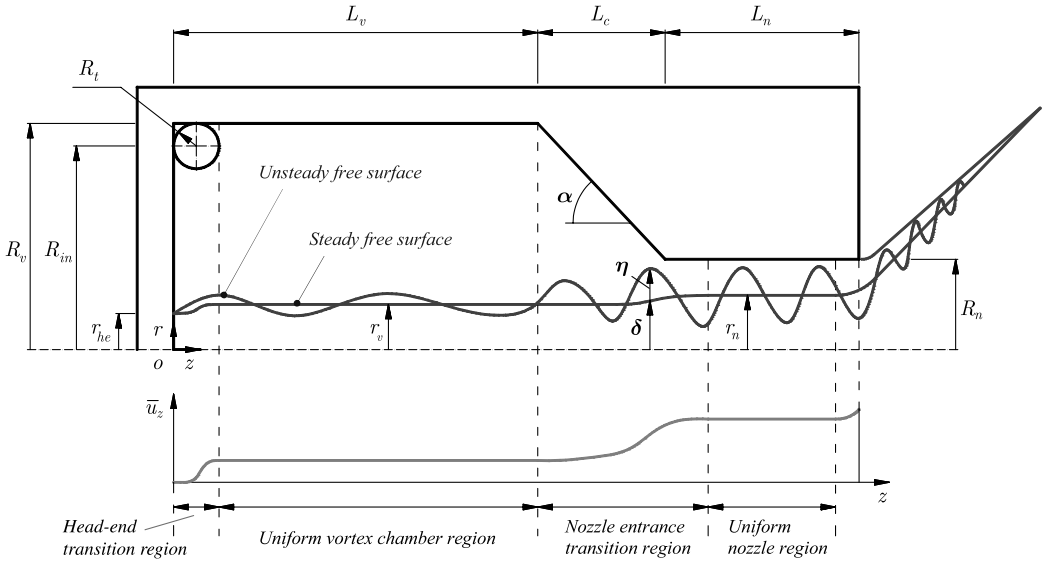

Fig. 1 Swirl injector flow schematic.

locations where the flow has discontinuities. For this purpose, in Sec. III, the expressions for the instantaneous mass flow rate and momentum fluctuation in terms of the disturbance frequency will be derived.

Both of these approximations are equally important, because each one of them may be used for the assessment of the swirl injector in terms of its resonant characteristics, depending on the level of detail required in the assessment. Also, they may serve as a cross check between each other, since this topic is new and the results have to be anchored to one another when possible.

Note that, in all models considered, we will assume that the circumferential velocity follows the free vortex law as $u_\theta = C/r$. Finally, we emphasize that we will deal with long waves only.

II. Fundamental Condition for Resonance from Wave Considerations

We know that a general swirl injector with an arbitrary angle of conical convergence generates an oblique reflection at the point where the vortex chamber connects to the conical section. For simplicity, let us imagine that we have placed a straight step discontinuity at that point so that all reflections in the vortex chamber become normal. Furthermore, let us completely disregard the part of the injector downstream of that step discontinuity. Figure 2 shows the assumed injector representation for this problem.

Now, let us imagine what the standing wave pattern would look like when the injector resonates with downstream processes (such as combustion). Consider vortex chamber resonance from the injector response perspective. First, we expect that at resonance, the injector response should be at its maximum. Second, from its definition (Bazarov [1]),

$$\Pi_{\text{inj}} = \frac{\dot{m}'_n/\bar{\dot{m}}_n}{\Delta p'_{\text{inj}}/\Delta \bar{p}_{\text{inj}}} \tag{1}$$

where $\dot{m}_n$ is the nozzle mass flow rate and Δp_{inj} is the injector pressure drop; we see that the injector response is maximized when the magnitude of the nozzle mass flow rate fluctuation $\dot{m}'_n$ is at its maximum and the magnitude of the injector pressure drop fluctuation $\Delta p'_{\text{inj}}$ is at its minimum. This is true if, and only if, we have a node at the head end and an antinode at the nozzle entrance [3] (Sec. 5.2). Figure 3 schematically shows different possible modes of the wave pattern that we may anticipate when the injector resonates.

In addition to the assumed radial step discontinuity, we also assume the following:

1) The disturbance wave speed is much larger than the axial bulk flow velocity in the vortex chamber, so we can think of the fluid in the vortex chamber as being quiescent with zero axial velocity, or $\bar{u}_{zv} = 0$ and $\mathrm{d}\bar{u}_{zv}/\mathrm{d}z = 0$.

2) Since the variation of the free surface radius at the head end is small [3] (Chap. 3), we can (overall) assume that $r_{\text{he}} = r_v$ (see Fig. 1).

In accordance with these assumptions, we can write the wave equation [1,14], which describes the height η of long waves traveling on the core of swirling fluid in the vortex chamber, as

$$\frac{\partial^2 \eta}{\partial t^2} = C^2 \frac{R_v^2 - r_v^2}{2r_v^4} \frac{\partial^2 \eta}{\partial z^2} \tag{2}$$

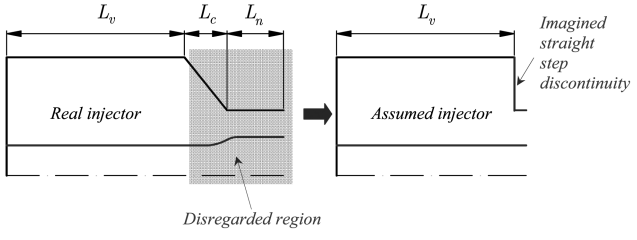

Fig. 2 Schematic of injector representation for ACRM.

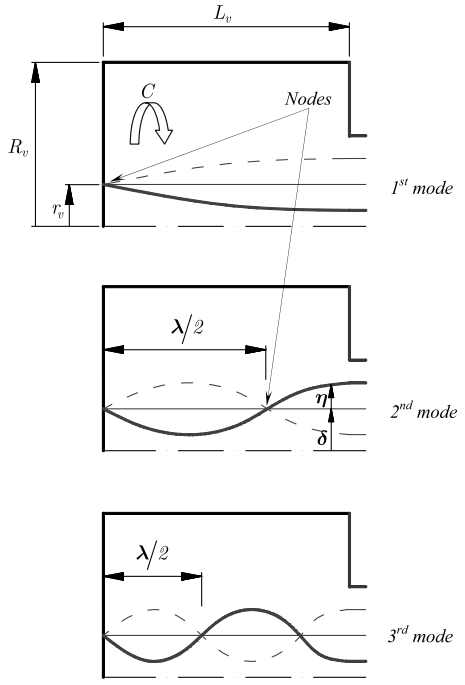

Fig. 3 Schematic of standing wave pattern when swirl injector is at resonance.

where the injector dimensions are shown in Figs. 1 and 3 and $C = u_\theta r$ is the angular momentum constant in the swirling flow. The general bounded solution to this equation is a periodic function,

$$\eta = [P\cos(k\gamma t) + Q\sin(k\gamma t)][A\cos(kz) + B\sin(kz)]$$

where P, Q, A, and B are the unknown constants, $\gamma^2 = C^2[(R_v^2 - r_v^2)/2r_v^4]$, and k is the wave number.

The positions of nodes and antinodes in Fig. 3 indicate two boundary conditions for η, valid at all times:

1) The condition $|\eta|$ should be zero at the head end, $z = 0$.

2) The condition $|\eta|$ should be maximum at the end of the vortex chamber, $z = L_v$.

From condition 1, we conclude that $A = 0$, which reduces the general solution to

$$\eta = [P\cos(k\gamma t) + Q\sin(k\gamma t)]\sin(kz)$$

where we have absorbed B into P and Q. Now, the standing wave pattern is clearly seen. From condition 2, we deduce that $\sin(kL_v) = \pm 1$, which yields the resonant wave numbers:

$$k = n\frac{\pi}{2L_v}, \qquad n = 1, 3, 5, \ldots \tag{3}$$

The resonant frequencies, $\omega_0 = k\gamma$, are

$$\omega_0 = n\frac{\pi}{2L_v}\sqrt{C^2\frac{R_v^2 - r_v^2}{2r_v^4}}, \qquad n = 1, 3, 5, \ldots \tag{4}$$

where the subscript zero emphasizes the notion of resonance.

III. Long-Wave Fluctuations of Mass Flow and Momentum in Cylindrical Flow Sections

In this section, based on the definitions of instantaneous mass flow rate and momentum, we will derive expressions for the fluctuating parts of each of them, written up to the first order in η, which are valid in a purely cylindrical section of the swirling flow in which the radii of steady flow boundaries and bulk stream velocity are considered constant and are experiencing long-wave perturbations. We need to know this information for use in the more precise wave reflection/

resonance models (ACRM and CCRM) of the swirl injector, which will come later in the next two sections.

Let us assume that we can split the axial flow velocity u_z and the cross-sectional area of the gaseous core A into the mean and disturbed parts as $u_z = \bar{u}_z + u'_z$ and $A = \bar{A} + A'$, respectively, where the disturbances are assumed small and given by Fourier waves

$$u'_z = \hat{u}_z e^{i(kz-\omega t)}, \qquad A' = \hat{A} e^{i(kz-\omega t)}, \qquad \eta = \hat{\eta} e^{i(kz-\omega t)}$$

Let us determine u'_z and A' in terms of η. From the definition of A,

$$A = \bar{A} + A' = \pi(\delta + \eta)^2 \simeq \pi\delta^2 + 2\pi\delta\eta$$

it follows that $A' = 2\pi\delta\eta$. To find u'_z, the cylindrical constant velocity flow setup assumed here permits us to use the linearized continuity equation by Darmofal et al. [15], which in combination with the expression for A', gives

$$u'_z = 2\delta \frac{k\bar{u}_z - \omega}{k(R^2 - \delta^2)} \eta \tag{5}$$

where δ is the steady free surface radius, and R is the solid boundary radius.

A. Long-Wave Fluctuation of Mass Flow Rate

By definition, the instantaneous mass flow rate at any flow cross section can be written as

$$\dot{m} = \rho \int_{\delta+\eta}^{R} (\bar{u}_z + u'_z) 2\pi r \, \mathrm{d}r = \rho \left[\int_{\delta}^{R} \bar{u}_z 2\pi r \, \mathrm{d}r - \int_{\delta}^{\delta+\eta} \bar{u}_z 2\pi r \, \mathrm{d}r + \int_{\delta}^{R} u'_z 2\pi r \, \mathrm{d}r - \int_{\delta}^{\delta+\eta} u'_z 2\pi r \, \mathrm{d}r \right]$$

Recognizing the steady mass flow rate in the first integral and neglecting the last integral (as it is a higher-order term), the unsteady part of the mass flow rate becomes

$$\dot{m}' = -2\pi\rho\delta\bar{u}_z\eta + \rho\pi(R^2 - \delta^2)u'_z$$

We can further modify this equation by substituting the velocity fluctuation from Eq. (5),

$$\dot{m}' = -2\pi\rho\delta \frac{\omega}{k} \eta \tag{6}$$

B. Long-Wave Fluctuation of Momentum

Assuming there are no external body or friction forces acting on the flow, we can define the total momentum of the flow, $M_\Sigma = \bar{M}_\Sigma + M'_\Sigma$, as composing the kinetic part, $M_u = \bar{M}_u + M'_u$, and the pressure part, $M_p = \bar{M}_p + M'_p$, which we may write as

$$M_\Sigma = M_u + M_p = \rho \int_{\delta+\eta}^{R} (\bar{u}_z + u'_z)^2 2\pi r \, \mathrm{d}r + \int_{\delta+\eta}^{R} p(r) 2\pi r \, \mathrm{d}r \tag{7}$$

Let us investigate both of these integrals separately. Starting from the kinetic part, we may write

$$M_u = \bar{M}_u + M'_u = \rho \int_{\delta+\eta}^{R} (\bar{u}_z + u'_z)^2 2\pi r \, \mathrm{d}r = \rho\bar{u}_z^2\pi(R^2 - \delta^2) - \rho\bar{u}_z^2\pi 2\delta\eta + \rho 2\bar{u}_z u'_z \pi(R^2 - \delta^2)$$

From here, we can extract the unsteady part and then substitute the velocity fluctuation from Eq. (5) as follows:

$$M'_u = -\rho 2\pi\delta\bar{u}_z^2\eta + \rho 2\pi(R^2 - \delta^2)\bar{u}_z u'_z = \rho\pi\left(-2\delta\bar{u}_z^2 + 4\bar{u}_z\delta\frac{k\bar{u}_z - \omega}{k}\right)\eta \tag{8}$$

Next, since the flow is purely axial and we do not have the radial velocity fluctuations in the long-wave treatment, the pressure at some radius in the flow may be written as

$$p(r) = \rho \int_{\delta+\eta}^{r} \frac{C^2}{\tilde{r}^3} \, \mathrm{d}\tilde{r} = \rho \frac{1}{2} C^2 \left[\frac{1}{(\delta+\eta)^2} - \frac{1}{r^2} \right]$$

where $\tilde{r}$ is a dummy radius. Now, we can insert this expression into the pressure part of momentum equation (7) to get

$$M_p = \bar{M}_p + M'_p = \int_{\delta+\eta}^{R} p(r) 2\pi r \, \mathrm{d}r = \rho\pi C^2 \left\{ \frac{1}{2} \frac{1}{(\delta+\eta)^2} [R^2 - (\delta+\eta)^2] - \ell_n \frac{R}{\delta+\eta} \right\} \tag{9}$$

To work on the first term in this expression, we will use the binomial expansion,

$$\frac{1}{(\delta+\eta)^2} \simeq \frac{1}{\delta^2} - \frac{2}{\delta^3}\eta$$

By substituting into the previous equation, we can write

$$\frac{1}{2} \frac{1}{(\delta+\eta)^2} [R^2 - (\delta+\eta)^2] = \frac{R^2 - \delta^2}{2\delta^2} - \frac{R^2 - \delta^2}{\delta^3}\eta - \frac{1}{\delta}\eta \tag{10}$$

To modify the logarithm term in Eq. (9), we will use the binomial expansion,

$$\frac{1}{\delta+\eta} \simeq \frac{1}{\delta} - \frac{1}{\delta^2}\eta$$

and the series expansion [16] (p. 111),

$$\ell_n x \simeq (x-1) - \frac{(x-1)^2}{2} + \frac{(x-1)^3}{3}$$

which we write up to the third term in this study. Note that this expansion is formally valid for $|x-1| \leq 1$ or $0 < x \leq 2$. In this study, for simplicity, we will assume that this series expansion is valid for the whole range of the argument, or for $x > 0$. Ideally, one would write as many terms in this expansion as possible to make the end result more precise. Then, the logarithmic term can be written as

$$\ell_n \frac{R}{\delta+\eta} = \left(\frac{R}{\delta} - 1\right) - \frac{1}{2}\left(\frac{R}{\delta} - 1\right)^2 + \frac{1}{3}\left(\frac{R}{\delta} - 1\right)^3 + \frac{R}{\delta^2}\left(-\frac{R^2}{\delta^2} + 3\frac{R}{\delta} - 3\right)\eta \tag{11}$$

Plugging Eqs. (10) and (11) back into the pressure part of momentum equation (9), we have

$$M_p = \rho\pi C^2 \left[\frac{R^2 - \delta^2}{2\delta^2} - \left(\frac{R}{\delta} - 1\right) + \frac{1}{2}\left(\frac{R}{\delta} - 1\right)^2 - \frac{1}{3}\left(\frac{R}{\delta} - 1\right)^3 \right] \cdots + \rho\pi C^2 \left[-\frac{R^2 - \delta^2}{\delta^3} - \frac{1}{\delta} - \frac{R}{\delta^2}\left(-\phi\frac{R^2}{\delta^2} + 3\frac{R}{\delta} - 3\right) \right] \eta$$

From here, we conclude that the unsteady part of the pressure momentum is given by

$$M'_p = \rho\pi C^2 \left[-\frac{R^2 - \delta^2}{\delta^3} - \frac{1}{\delta} - \frac{R}{\delta^2}\left(-\frac{R^2}{\delta^2} + 3\frac{R}{\delta} - 3\right) \right] \eta = \rho\pi C^2 \frac{1}{\delta^4}(R^3 - 4R^2\delta + 3R\delta^2)\eta \tag{12}$$

Adding the unsteady kinetic and pressure parts given by Eqs. (8) and (12) and rearranging, we arrive at the expression for the total momentum fluctuation:

$$M'_{\Sigma} = \rho\pi\left[-2\delta\bar{u}_z^2 + 4\bar{u}_z\delta\frac{k\bar{u}_z-\omega}{k} + C^2\frac{1}{\delta^4}(R^3 - 4R^2\delta + 3R\delta^2)\right]\eta \tag{13}$$

IV. Abrupt Convergence Resonance Model: Wave Reflections and Resonance with Abrupt Step Discontinuity

In this section, let us build upon the previously mentioned idea that we have an abrupt step change at the end of the vortex chamber and connect the nozzle just downstream of that step, with its own solid boundary and free surface radii, R_n and r_n, respectively (Fig. 4). Consider an incident downstream traveling wave, $D\exp[i(k_2 z - \omega t)]$, in the vortex chamber. When it comes to the step discontinuity, a part of it reflects back as an upstream traveling wave, $B\exp[i(k_1 z - \omega t)]$, and another part of it propagates further into the nozzle as a transmitted downstream traveling wave, $A\exp[i(k_n z - \omega t)]$. The arrows in Fig. 4 indicate the respective directions in which all of these waves travel, and k_1, k_2, and k_n denote the corresponding wave numbers. Here, and further on, the upstream traveling waves will be indicated by odd numbers and the downstream traveling waves by even numbers. Note that there may not exist an upstream traveling wave in the nozzle, as the local flow speed typically exceeds the upstream wave speed. Finally, similar to Sec. II, we will assume again that the bulk flow axial velocity in the vortex chamber is negligibly smaller in comparison with the disturbance wave speed and may be set to zero, $\bar{u}_{zv} = 0$.

Based on Eq. (5), at any point in the vortex chamber, we may write the collective velocity fluctuation of the waves B and D, which are superposed on each other, as

$$u'_z = 2r_v\left[\frac{k_1\bar{u}_{zv}-\omega}{k_1(R_v^2 - r_v^2)}Be^{i(k_1 z-\omega t)} + \frac{k_2\bar{u}_{zv}-\omega}{k_2(R_v^2 - r_v^2)}De^{i(k_2 z-\omega t)}\right]$$

At the head-end solid wall, $z = 0$, we know that the axial velocity fluctuation should be zero at all times. Then, noting that $\bar{u}_{zv} = 0$, we can reduce this equation to

$$u'_z(0,t) = \frac{B}{k_1} + \frac{D}{k_2} = 0$$

Again, since $\bar{u}_{zv} = 0$, the wave numbers k_1 and k_2 are symmetrical, $k_1 = -k_2$. But, based on the last equation, this means that $D = B$. Conclusively, we can say that we have a purely standing wave in the vortex chamber, which excites an outgoing wave of amplitude A in the nozzle.

To relate A to the amplitude of the standing wave in the vortex chamber D, consider the balance of the mass flow rate fluctuation at the matching boundary, $z = L_v$ (see Fig. 4). Based on the derived equation (6) for the mass flow rate fluctuation, we may write

$$-2\pi\rho r_v\left[\frac{\omega}{k_1}Be^{i(k_1 L_v-\omega t)} + \frac{\omega}{k_2}De^{i(k_2 L_v-\omega t)}\right] = -2\pi\rho r_n\frac{\omega}{k_n}Ae^{i(k_n L_v-\omega t)}$$

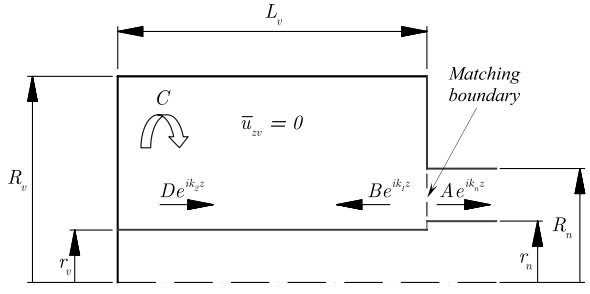

Fig. 4 Schematic of wave reflection and transmission for ACRM.

By substituting the equalities $D = B$ and $k_1 = -k_2$, and rearranging, we can obtain the expression for A in terms of D:

$$A = \frac{(r_v/k_2)(e^{-ik_2 L_v} - e^{ik_2 L_v})}{-(r_n/k_n)e^{ik_n L_v}}D \tag{14}$$

What does this equation mean from the injector resonance point of view? In this equation, k_2 and k_n depend on the disturbance frequency through the long-wave speed relationship, given in general as

$$\omega - k\bar{u}_z = \pm k\sqrt{C^2\frac{R^2-\delta^2}{2\delta^4}} \tag{15}$$

and which, for the vortex chamber and the nozzle, is given by

$$\omega = +k_2\sqrt{C^2\frac{R_v^2 - r_v^2}{2r_v^4}}, \qquad \omega - k_n\bar{u}_{zn} = +k_n\sqrt{C^2\frac{R_n^2 - r_n^2}{2r_n^4}}$$

These equations take into account the respective film thicknesses in the vortex chamber, $R_v - r_v$, and the nozzle, $R_n - r_n$. Hence, if D is fixed in Eq. (14), the magnitude of A should vary with regard to ω. Then, there may be frequencies where $|A|$ is maximized, thereby causing the most pronounced mass flow rate pulsation in the nozzle. Theoretically, these frequencies should coincide with the resonant frequencies [Eq. (4)], which we have previously derived in the fundamental condition for resonance (Sec. II).

V. Conical Convergence Resonance Model: Wave Reflections and Resonance with Conical Convergence Section

Let us add some of the more realistic features to the previous model by considering that there are the following additional components of the injector flow:

1) A distinct head-end region, $0 < z < 2R_t$, where the bulk flow velocity is zero and the free surface radius is equal to r_v, as shown in Fig. 1.

2) A nonzero bulk flow velocity in the vortex chamber, in the region $2R_t < z < L_v$.

3) A distinct conical convergence section connecting the vortex chamber to the nozzle, spanning the region $L_v < z < L_v + L_c$.

Item 1 tells us that, now, we can have a purely standing wave only in the head-end region of the flow. Item 2 will result in the fact that, because there is now a finite bulk flow velocity in the vortex chamber, the lengths of the waves propagating in streamwise and counter-streamwise directions will differ from each other, which leads to the phenomenon of partial standing waves, which is well described in Dean and Dalrymple [17]. Item 3 invokes the notion of a smooth variation of bulk flow velocity and boundaries in the conical convergence region up to the point where the free surface radius reaches the value of r_n in the nozzle. The nonuniform flow causes the disturbance waves to both refract and reflect as they travel through the flow transition.

This compound problem of wave refraction and reflection is difficult to attack at once. However, there is a simplifying way to deal with it by saying that we can discretize the entire transition region into short cylindrical sections in which the radii of solid and free surface boundaries do not change, thereby effectively eliminating refraction. This technique is very similar to that used in gravity waves, where the classic example is the paper by O'Hare and Davies [18]. But, in each of these short sections, we need to know the local wave number. It can be shown (see [3], Sec. 4.2) that the same long-wave equation (15) can be used in this case, with the difference that the local values of $\bar{u}_z$, R, and δ need to be used. In turn, the local bulk flow velocity simply follows from the steady-state continuity in each of these sections.

We will start the analysis by first considering that there is just one cylindrical section connecting the vortex chamber to the nozzle. This

will serve as a good platform to show the main features of the problem. Then, we will generalize the equations used in this simple problem for further use in geometries where more transition sections are considered. The analysis will be concluded with an algorithm that produces solutions for such general geometries.

A. Conical Convergence Resonance Model with One Cylindrical Section in Transition

For now, let us represent the transition region by just one cylindrical section, as shown in Fig. 5. The flow parameters corresponding to this cylindrical section will be denoted by the subscript 2 to indicate that it is located next to the nozzle section. Further, let the radii of this cylindrical section be given as the average between the corresponding solid boundary and free surface radii of the vortex chamber and the nozzle: $R_2 = (R_v + R_n)/2$ and $r_2 = (r_v + r_n)/2$. We have four sections of the flow connected at their respective discontinuity boundaries: the head-end region, the uniform vortex chamber region, the cylindrical section, and the nozzle. Note that we consider the nozzle up to the point where we assume the transition ends, which based on the results of [3] (Sec. 3.4), is located at $z = L_v + L_c + 0.5R_n$ (see Fig. 5).

Similar, to the previous ACRM, if an incident wave $M\exp[i(k_8 z - \omega t)]$ has originated, say, at the head end, it will generate a series of reflected and transmitted waves in all of these four flow sections. Figure 5 shows their respective directions of propagation and wave numbers. In each section, we have two waves traveling in opposite directions. We can calculate their wave numbers, but their amplitudes are unknown. Let us say that we know the amplitude of the original incident wave M. Since there is a purely standing wave at the head end, then we also know that $N = M$ and $k_7 = -k_8$ (see Sec. IV for more discussion). This leaves us with six unknown amplitudes: A through G. There are three matching discontinuity boundaries that can relate them together, with locations at: $z = 2R_t$, $z = L_v$, and $z = L_v + L_c$. In contrast with the previous ACRM, at each of these boundaries, in addition to the matching of the fluctuating mass flow rate, we will also assure the matching of the fluctuating momentum. This will, accordingly, provide six equations to solve for the unknown wave amplitudes.

Let us start with matching the fluctuating mass flow rate given by Eq. (6) at $z = 2R_t$, $z = L_v$, and $z = L_v + L_c$. Then, we can write the following:

$$-\frac{\omega}{k_5}Fe^{ik_5 2R_t} - \frac{\omega}{k_6}Ge^{ik_6 2R_t} = \frac{\omega}{k_8}(e^{-ik_8 2R_t} - e^{ik_8 2R_t})M \tag{16}$$

$$-r_2\frac{\omega}{k_3}De^{ik_3 L_v} - r_2\frac{\omega}{k_4}Ee^{ik_4 L_v} + r_v\frac{\omega}{k_5}Fe^{ik_5 L_v} + r_v\frac{\omega}{k_6}Ge^{ik_6 L_v} = 0 \tag{17}$$

$$-r_n\frac{\omega}{k_1}Ae^{ik_1(L_v+L_c)} - r_n\frac{\omega}{k_2}Be^{ik_2(L_v+L_c)} + r_2\frac{\omega}{k_3}De^{ik_3(L_v+L_c)} + r_2\frac{\omega}{k_4}Ee^{ik_4(L_v+L_c)} = 0 \tag{18}$$

Before considering matching the fluctuating momentum, let us introduce the following coefficients:

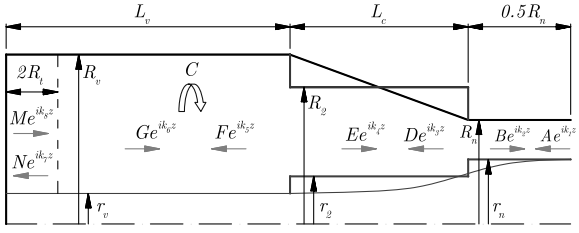

Fig. 5 Schematic of wave reflection and transmission for CCRM with one cylindrical section.

$$K_A = -2r_n\bar{u}_{zn}^2 + 4\bar{u}_{zn}r_n\frac{k_1\bar{u}_{zn} - \omega}{k_1} + C^2\frac{1}{r_n^4}(R_n^3 - 4R_n^2 r_n + 3R_n r_n^2)$$

$$K_B = -2r_n\bar{u}_{zn}^2 + 4\bar{u}_{zn}r_n\frac{k_2\bar{u}_{zn} - \omega}{k_2} + C^2\frac{1}{r_n^4}(R_n^3 - 4R_n^2 r_n + 3R_n r_n^2)$$

$$K_D = -2r_2\bar{u}_{z2}^2 + 4\bar{u}_{z2}r_2\frac{k_3\bar{u}_{z2} - \omega}{k_3} + C^2\frac{1}{r_2^4}(R_2^3 - 4R_2^2 r_2 + 3R_2 r_2^2)$$

$$K_E = -2r_2\bar{u}_{z2}^2 + 4\bar{u}_{z2}r_2\frac{k_4\bar{u}_{z2} - \omega}{k_4} + C^2\frac{1}{r_2^4}(R_2^3 - 4R_2^2 r_2 + 3R_2 r_2^2)$$

$$K_F = -2r_v\bar{u}_{zv}^2 + 4\bar{u}_{zv}r_v\frac{k_5\bar{u}_{zv} - \omega}{k_5} + C^2\frac{1}{r_v^4}(R_v^3 - 4R_v^2 r_v + 3R_v r_v^2)$$

$$K_G = -2r_v\bar{u}_{zv}^2 + 4\bar{u}_{zv}r_v\frac{k_6\bar{u}_{zv} - \omega}{k_6} + C^2\frac{1}{r_v^4}(R_v^3 - 4R_v^2 r_v + 3R_v r_v^2)$$

Then, based on Eq. (13), the matching equations for the fluctuating momentum at $z = 2R_t$, $z = L_v$, and $z = L_v + L_c$ are given by

$$K_F Fe^{ik_5 2R_t} + K_G Ge^{ik_6 2R_t} = C^2\frac{1}{r_v^4}(R_v^3 - 4R_v^2 r_v + 3R_v r_v^2)(e^{-ik_8 2R_t} + e^{ik_8 2R_t})M \tag{19}$$

$$K_D De^{ik_3 L_v} + K_E Ee^{ik_4 L_v} - K_F Fe^{ik_5 L_v} - K_G Ge^{ik_6 L_v} = 0 \tag{20}$$

$$K_A Ae^{ik_1(L_v+L_c)} + K_B Be^{ik_2(L_v+L_c)} - K_D De^{ik_3(L_v+L_c)} - K_E Ee^{ik_4(L_v+L_c)} = 0 \tag{21}$$

We can rewrite Eqs. (16–21) in a matrix form. as shown in Fig. 6. Solution of this matrix equation then gives the dependence of the wave amplitudes A through G on the wave amplitude of the original incident wave M.

What information can we extract from this solution with regard to the injector resonance? As before, all wave numbers in the matrix equation (Fig. 6) depend on the disturbance frequency ω. Therefore, all amplitudes A through G in the solution depend on ω as well. At injector resonance, because the film thickness fluctuation in the injector nozzle should be maximum, we should see the greatest magnitude of the disturbance wave transmitted into the nozzle, which is represented by the amplitude B and vice versa; we should see the smallest magnitude of the disturbance wave traveling back into the vortex chamber, which is represented by amplitude A. Accordingly, the frequency at which $|B|$ is maximum indicates a resonant frequency.

B. Generalization of Conical Convergence Resonance Model to Multiple Cylindrical Sections in Transition

We are interested in having multiple cylindrical sections in the transition region in order to better represent a conical convergence surface. This will generate a larger matrix than that shown in Fig. 6 for finding all wave amplitudes involved in the solution. Let the solution in this case be represented by a matrix equation $X \cdot a = Y$, where X and Y are the generic matrices similar to the left-hand side and the right-hand side matrices in Fig. 6, and a are the generic wave amplitudes. To illustrate how to construct the matrices X and Y, let us consider again the flow setup that has just one cylindrical section in conical transition as a reference (Fig. 7). This will serve as a starting platform from where the solution may be extended further onto more transition sections.

Let us represent each flow section by an index q and their total number by N. Let the head-end section be denoted by the index $q = N + 1$. In this particular case, $N = 3$ and $q = 1, \ldots, 4$. Let the first index under the wave number correspond to the flow section number and the second index to the direction of wave propagation: 1 is for upstream-traveling waves, and 2 is for downstream-traveling waves. Moreover, let us define the radial boundaries of each section by r_q and R_q and the discontinuity boundaries, at which the flow

$$\begin{pmatrix} -r_n\frac{\omega}{k_1}e^{ik_1(L_v+L_c)} & -r_n\frac{\omega}{k_2}e^{ik_2(L_v+L_c)} & r_2\frac{\omega}{k_3}e^{ik_3(L_v+L_c)} & r_2\frac{\omega}{k_4}e^{ik_4(L_v+L_c)} & 0 & 0 \\ 0 & 0 & -r_2\frac{\omega}{k_3}e^{ik_3L_v} & -r_2\frac{\omega}{k_4}e^{ik_4L_v} & r_v\frac{\omega}{k_5}e^{ik_5L_v} & r_v\frac{\omega}{k_6}e^{ik_6L_v} \\ 0 & 0 & 0 & 0 & -\frac{\omega}{k_5}e^{ik_52R_t} & -\frac{\omega}{k_6}e^{ik_62R_t} \\ K_Ae^{ik_1(L_v+L_c)} & K_Be^{ik_2(L_v+L_c)} & -K_De^{ik_3(L_v+L_c)} & -K_Ee^{ik_4(L_v+L_c)} & 0 & 0 \\ 0 & 0 & K_De^{ik_3L_v} & K_Ee^{ik_4L_v} & -K_Fe^{ik_5L_v} & -K_Ge^{ik_6L_v} \\ 0 & 0 & 0 & 0 & K_Fe^{ik_52R_t} & K_Ge^{ik_62R_t} \end{pmatrix} \begin{pmatrix} A \\ B \\ D \\ E \\ F \\ G \end{pmatrix} =$$

$$\begin{pmatrix} 0 \\ 0 \\ \frac{\omega}{k_8}\left(e^{-ik_82R_t}-e^{ik_82R_t}\right) \\ 0 \\ 0 \\ C^2\frac{1}{r_v^4}\left(R_v^3-4R_v^2r_v+3R_vr_v^2\right)\left(e^{-ik_82R_t}+e^{ik_82R_t}\right) \end{pmatrix} M$$

Fig. 6 Representation of Eqs. (16–21) in matrix form for CCRM with one cylindrical section.

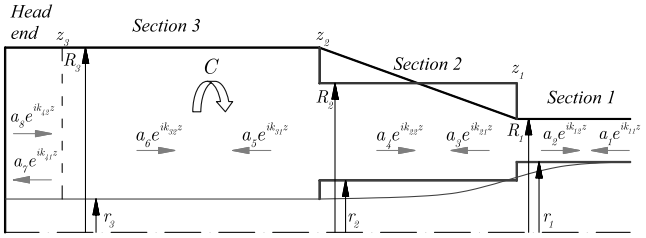

Fig. 7 Schematic of wave reflection and transmission for generic CCRM.

sections connect to each other, by z_q. Finally, note that the wave amplitudes a are counted simply in a sequence (1, 2, 3, ...).

By comparing Fig. 7 to Fig. 5, it is easy to determine r_q, R_q, and z_q; they are summarized in Table 1. Based on r_q and R_q, we can determine the bulk flow velocity $\bar{u}_{zq}$, the wave numbers k_q, and the coefficients K_q (which are needed for the momentum balance; see page 6) for each section of the flow. The bulk flow velocity follows from the one-dimensional continuity as

$$\bar{u}_{zq} = \bar{u}_{zv}\frac{R_v^2 - r_v^2}{R_q^2 - r_q^2} \tag{22}$$

The wave numbers for both upstream- and downstream-traveling waves can be found, based on Eq. (15), as

$$k_{q,1} = \omega\frac{\bar{u}_{zq} + \sqrt{C^2[(R_q^2 - r_q^2)/2r_q^4]}}{\bar{u}_{zq}^2 - C^2[(R_q^2 - r_q^2)/2r_q^4]} \tag{23}$$

$$k_{q,2} = \omega\frac{\bar{u}_{zq} - \sqrt{C^2[(R_q^2 - r_q^2)/2r_q^4]}}{\bar{u}_{zq}^2 - C^2[(R_q^2 - r_q^2)/2r_q^4]} \tag{24}$$

and by using Eqs. (22–24), we can determine the coefficients K as

Table 1 Values of r_q, R_q, and z_q in generic CCRM with one cylindrical section

$r_1 = r_n$	$R_1 = R_n$	$z_1 = L_v + L_c$
$r_2 = (r_v + r_n)/2$	$R_2 = (R_v + R_n)/2$	$z_2 = L_v$
$r_3 = r_v$	$R_3 = R_v$	$z_3 = 2R_t$
$r_4 = r_v$	$R_4 = R_v$	$z_4 = 0$

$$K_{q,1} = -2r_q\bar{u}_{zq}^2 + 4\bar{u}_{zq}r_q\frac{k_{q,1}\bar{u}_{zq} - \omega}{k_{q,1}} + C^2\frac{1}{r_q^4}(R_q^3 - 4R_q^2r_q + 3R_qr_q^2) \tag{25}$$

$$K_{q,2} = -2r_q\bar{u}_{zq}^2 + 4\bar{u}_{zq}r_q\frac{k_{q,2}\bar{u}_{zq} - \omega}{k_{q,2}} + C^2\frac{1}{r_q^4}(R_q^3 - 4R_q^2r_q + 3R_qr_q^2) \tag{26}$$

Now, we can rewrite the matrix equation shown in Fig. 6 in the terms r_q, z_q, k_q, and K_q, as given in Fig. 8. Similar to the previous matrix solution, the resonance will follow from this solution at frequencies where $|a_2|$ is at its maximum.

An algorithm has been created ([3], Sec. 5.5) to construct the matrices like the one shown in Fig. 8. The matrix is divided into halves, resulting from mass flow and momentum conditions, respectively, and constructed following standard linear algebra techniques. Solutions have been obtained for a general number of steps, as described in the following section. As a validation of this algorithm, we confirmed that it replicated the results obtained in the previous section when only a single step was present.

VI. Nondimensionalization and Baseline Injector

In this study, we will use the fluid density ρ^*, nozzle radius R_n^*, and mean tangential inlet inflow velocity $\bar{W}_{\text{in}}^*$ as dimensions. The dimensional values are denoted by superscript *. Hence, for the parameters that we will use further on, we have

$$\omega^* = \omega\frac{\bar{W}_{\text{in}}^*}{R_n^*}, \qquad k^* = k\frac{1}{R_n^*}, \qquad C^* = C\bar{W}_{\text{in}}^*R_n^*$$

Since, eventually, in Part II [19] of this research, we will validate theoretical results in this study against Ahn's [10] experimental results, the baseline injector will have the same characteristics as the injector used in his experimental testing ([10], App. B), with the sizes outlined in Table 2.

The baseline steady-state pressure drop and convergence angle are $\Delta\bar{p}_{\text{inj}} = 40.3$ psi and $\alpha = 45°$. Applying the methodology described in Bazarov [1] (Sec. 3.1), we can calculate the steady core radii and velocities (Table 3).

$$\begin{pmatrix} -r_1\frac{\omega}{k_{1,1}}e^{ik_{1,1}z_1} & -r_1\frac{\omega}{k_{1,2}}e^{ik_{1,2}z_1} & r_2\frac{\omega}{k_{2,1}}e^{ik_{2,1}z_1} & r_2\frac{\omega}{k_{2,2}}e^{ik_{2,2}z_1} & 0 & 0 \\ 0 & 0 & -r_2\frac{\omega}{k_{2,1}}e^{ik_{2,1}z_2} & -r_2\frac{\omega}{k_{2,2}}e^{ik_{2,2}z_2} & r_3\frac{\omega}{k_{3,1}}e^{ik_{3,1}z_2} & r_3\frac{\omega}{k_{3,2}}e^{ik_{3,2}z_2} \\ 0 & 0 & 0 & 0 & -\frac{\omega}{k_{3,1}}e^{ik_{3,1}z_3} & -\frac{\omega}{k_{3,2}}e^{ik_{3,2}z_3} \\ K_{1,1}e^{ik_{1,1}z_1} & K_{1,2}e^{ik_{1,2}z_1} & -K_{2,1}e^{ik_{2,1}z_1} & -K_{2,2}e^{ik_{2,2}z_1} & 0 & 0 \\ 0 & 0 & K_{2,1}e^{ik_{2,1}z_2} & K_{2,2}e^{ik_{2,2}z_2} & -K_{3,1}e^{ik_{3,1}z_2} & -K_{3,2}e^{ik_{3,2}z_2} \\ 0 & 0 & 0 & 0 & K_{3,1}e^{ik_{3,1}z_3} & K_{3,2}e^{ik_{3,2}z_3} \end{pmatrix} \begin{pmatrix} a_1 \\ a_2 \\ a_3 \\ a_4 \\ a_5 \\ a_6 \end{pmatrix} =$$

$$\begin{pmatrix} 0 \\ 0 \\ \frac{\omega}{k_{4,2}}\left(e^{-ik_{4,2}z_3} - e^{ik_{4,2}z_3}\right) \\ 0 \\ 0 \\ C^2\frac{1}{r_4^4}\left(R_4^3 - 4R_4^2r_4 + 3R_4r_4^2\right)\left(e^{-ik_{4,2}z_3} + e^{ik_{4,2}z_3}\right) \end{pmatrix} a_8$$

Fig. 8 Matrix form of solution for generic CCRM with one cylindrical section.

VII. Results

In this section, the results will be presented for each of the previously derived models of the wave reflection and resonance. Both ACRM and CCRM are compared against the fundamental condition for the resonance shown in Eq. (4). All results presented here are valid for the baseline injector described in Tables 2 and 3.

A. Abrupt Convergence Resonance Model Results

From Eq. (4), we can immediately determine the resonant frequencies. A practical issue results from the fact that the ACRM presumes a radial step, while the actual injector incorporates a conical convergence. For the purposes of comparison, we shall assume that the step is located at the center of the convergence section, which implies that we replace the vortex chamber length in Eq. (4) with the length $L_v + L_c/2$, where L_c is the length of the convergence section. We shall apply this methodology throughout as we assess the behavior of the ACRM.

Table 2 Baseline injector geometry

Parameter	Dimensional, in.	Nondimensional
R_n	0.250	1.0
R_{in}	1.125	4.5
R_t	0.125	0.5
R_v	1.250	5.0
L_t	0.450	1.8
L_n	1.000	4.0
L_v	5.000	20.0
N_{in}		4

Table 3 Baseline steady core radii and flow velocities

Parameter	Dimensional	Nondimensional
r_{he}	0.1794 in	0.7177
r_v	0.1794 in	0.7177
r_n	0.2019 in	0.8077
$\bar{W}_{\text{in}}$	3.7596 m/s	1.0
$\bar{u}_{zv}$	0.1535 m/s	0.0408
$\bar{u}_{zn}$	10.8135 m/s	2.8762

For the baseline injector, we have summarized them in Table 4 for the first five modes. Notice that, due to this calculation, the first resonant frequency is 205.7 Hz, to which we will refer to in Part II of this research [19] when comparing with the experimental first resonant frequency.

We set the amplitude of the incident wave at the head end to unity, $D = 1$. Then, based on Eq. (14), we plotted the amplitude (absolute value) of the outgoing wave $|A|$ versus the disturbance frequency (Fig. 9). Notice that the peaks of $|A|$ are located exactly at the same frequencies as was predicted by the fundamental resonance condition (see Table 4). As was assumed in ACRM, these peaks indicate the frequencies at which the mass flow rate pulsation in the nozzle becomes maximum; hence, they are the resonant peaks.

This calculation also shows that the value of $|A|$ varies from 0 to 9.45. The fact that $|A|$ shrinks to zero at some frequencies tells us that, at these frequencies, we can potentially expect damping of flow pulsations in the injector. Furthermore, the fact that $|A|$ may reach values as large as 9.45, compared with the value of $D = 1$, signifies that the amplitudes of the outgoing waves may be much larger than the amplitudes of the original incident waves in the vortex chamber. This situation is natural, because we know that the wavelength in the nozzle is shorter than in the vortex chamber; thus, the wave amplitude has to be larger to conserve energy.

B. Conical Convergence Resonance Model Results

From the way the CCRM is derived, we can raise the question of how many short cylindrical sections there should be in the transition region. In other words, what does short mean in relation to the axial dimension of the transition? We can deal with this problem as follows. We will investigate several different setups, with a different number of cylindrical sections in the transition in each case, in terms of the resonant peaks that each of them produces. Note that increasing the number of cylindrical sections leads to larger solution

Table 4 Resonant frequencies due to ACRM (first five modes)

Mode, n	ω_0	ω_0^*, rad/s	f_0^*, Hz
1	2.2	1292.2	205.7
3	6.5	3876.7	617.0
5	10.9	6461.1	1028.3
7	15.3	9045.5	1439.6
9	19.6	11630.0	1851.0

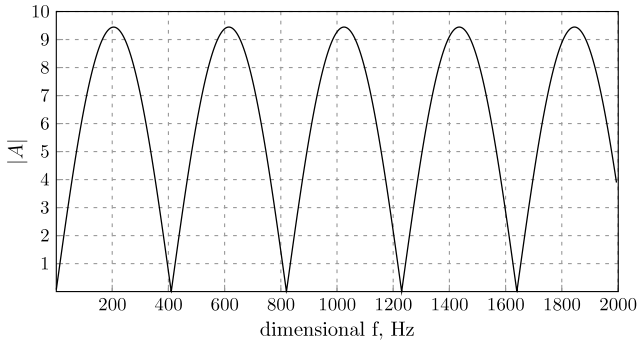

Fig. 9 Amplitude of the outgoing wave vs disturbance frequency in ACRM.

matrices, which increases the computational time. If there is a large variation in the answer from case to case, we should be looking for a converged solution. If the answer does not change much, then we can choose the setup that is the fastest.

Let us first consider eight cylindrical sections in the transition (Fig. 10). This corresponds to the length of each of these sections equal to $0.5R_n$. The amplitude of the original incident wave at the head end is set to one, as before. For this setup, the amplitude of the outgoing wave a_2 (see Fig. 7) versus the disturbance frequency is shown in Fig. 11. Notice that the resonant peaks, now located at 118 and 470 Hz, are different from the first two resonant peaks, 205 and 617 Hz, predicted by ACRM (see Table 4 and Fig. 9). This immediately indicates that the resonant characteristics of an injector

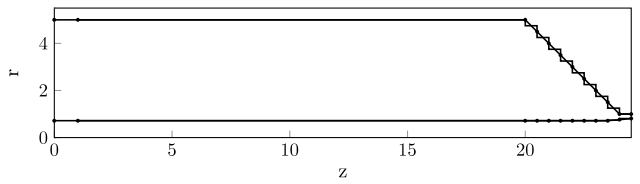

a) Normal view

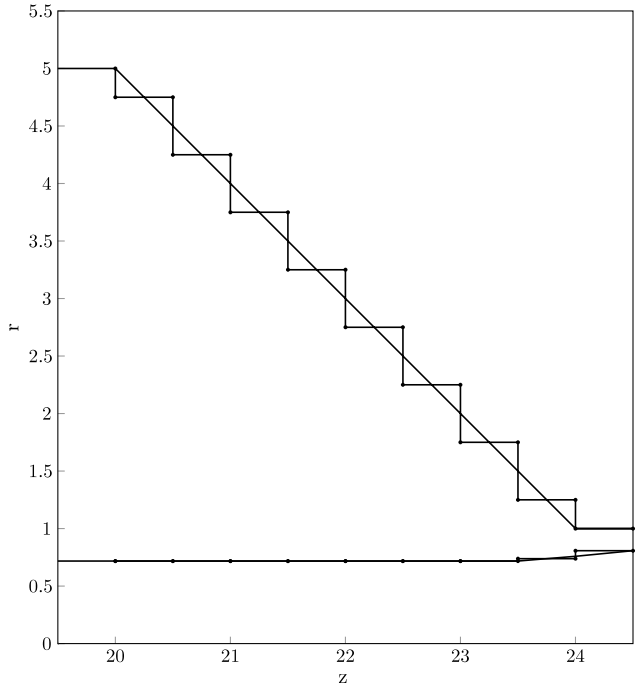

b) Zoomed in view

Fig. 10 Example of eight cylindrical sections in transition, considered for wave reflections in CCRM.

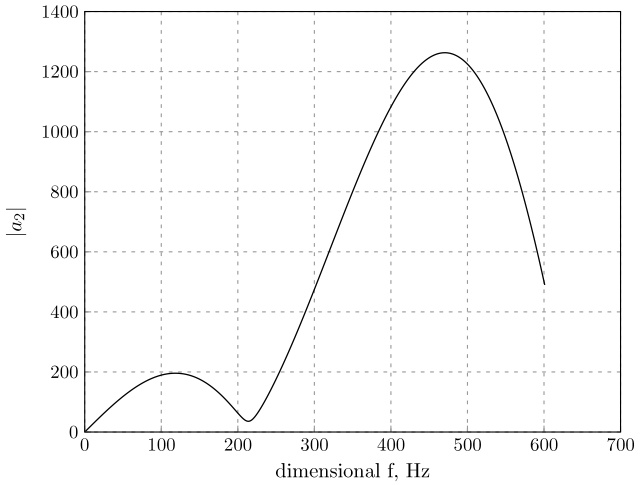

Fig. 11 Outgoing wave amplitude vs disturbance frequency for CCRM with eight cylindrical sections in transition (peaks at 118 and 470 Hz).

with a distinct conical convergence section do differ from those of an injector with a 90° step transition. Also, by looking at the magnitude of $|a_2|$ at different frequencies (which reaches the value of 1263 at the second peak) in relation to the magnitude of the original incident wave (which is one), one may wonder why the former is so much larger. The answer follows from the fact that the amplitude of the upstream traveling waves rises to infinity as we move closer to the point where the transition ends and the uniform nozzle region starts (see [3], Chap. 4). This fact causes the large difference between the amplitudes of the original incident waves and the outgoing waves. Since, after all, this analysis is a first-order small disturbance analysis, the wave amplitudes are not as important as the frequencies where they peak out.

Now, let us move on to the larger number of cylindrical sections by decreasing their width down to 5% of the previous width $0.5R_n$. The width is denoted as w in this investigation. Figure 12 shows the new locations of the resonant peaks, and Table 5 summarizes the respective resonant frequencies along with the sizes of the solution matrices in each of the cases considered.

In Table 5, we can see that the resonant peaks are moving within 3% of the baseline values as we vary w. The solution matrices, however, grow roughly two times bigger each time we decrease the width to half of the previous. This means that we can choose the baseline case, with $w = 0.5R_n$, for further calculations, because it requires the least computational time.

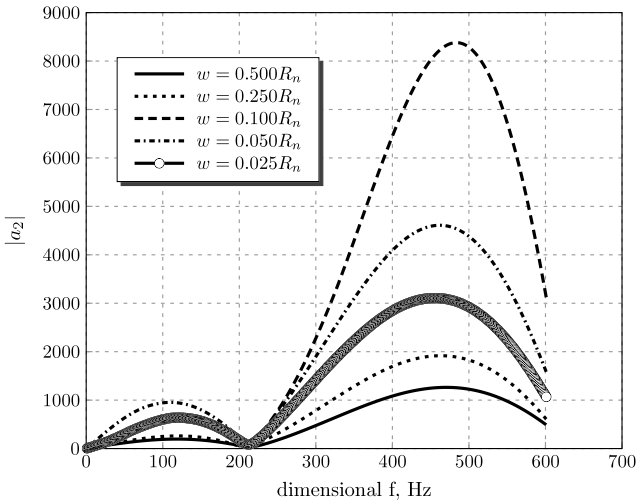

Fig. 12 Sensitivity of outgoing wave amplitude to cylindrical section width in CCRM (resonant peaks are summarized in Table 5).

Table 5 Sensitivity of resonant peaks in CCRM to cylindrical section width

Width, w	First peak, Hz	Second peak, Hz	Solution matrix size
$0.500R_n$	118	470	10×10
$0.250R_n$	119	463	19×19
$0.100R_n$	121	484	46×46
$0.050R_n$	110	462	91×91
$0.025R_n$	120	455	181×181

VIII. Conclusions

In this paper, the possible methods of accounting for disturbance wave reflections and the resonance caused by them in the rocket swirl injector were presented. Two models were considered that differed in their levels of complexity; the presence of the nozzle and the treatment of the exact connection of the nozzle to the vortex chamber were considered, through sudden step discontinuity or the conical convergence section.

The results following from the first abrupt convergence resonance model (ACRM) have shown the same resonant frequency predicted by a simple wave analysis [Eq. (4)], which confirms the existence of resonant frequencies within a swirl injector. Because both of them only take into account a sudden step discontinuity, it can potentially be expected that both of them can be used for the resonance analysis of the injectors having 90° sudden convergence or steep convergence angles, in general.

From the results of CCRM, it has been seen that the amplitude of the outgoing wave can be much larger than the amplitude of the incident wave. This is attributed to the fact that the amplitude of the upstream traveling wave, at the point where the nozzle entrance transition region ends and the uniform nozzle region begins, grows to infinity, as follows from [3] (Chap. 4). It has also been seen that the resonant frequencies following from the CCRM are different from those in ACRM. This clearly shows that, when the injector has a distinct conical convergence between the vortex chamber and the nozzle, its wave reflection and resonance characteristics are different from the injector having the 90° sudden step convergence.

Now, the question is: can these models be trusted to predict the injector resonance? The approach to answer this question will involve setting up a computational BEM model in Part II of this study [19], which closely replicates the boundary conditions used in the analytic models here, and going through the parametric study, in which the influences of such parameters as α, L_v, L_n, R_v, and $\bar{W}_{\text{in}}$ on the injector response can be investigated. The comparison of the frequencies where the response is maximized with the resonant frequencies predicted by the analytic models in this part of the study will provide an indication of how adequate they are. Following this logic, in Part II [19], both the theoretical and computational results will be presented in parallel. Ultimately, the theoretical and computational results will be compared to the experimental. While there are limited data for this comparison, this will also be addressed in Part II [19].

To conclude, it has to be noted that, in such reflection–refraction problems, where the transition is approximated by the cylindrical sections in addition to the regular linear reflected and transmitted waves, other types of waves would be expected to form that would damp out as they propagated far away from their respective step discontinuities. But usually, the required analysis applies a variational approach, a classic gravity wave demonstration of which is provided in Miles [20]. In this study, these waves have been ignored, as the application of variational analysis to the swirling flow is difficult. But their inclusion could potentially make the reflection/resonance analysis presented here more precise.

Acknowledgments

This research was supported by the U.S. Air Force Office of Scientific Research and Mitat Birkan under contract number FA9550-08-1-0115.

References

[1] Bazarov, V. G., *Liquid Injector Dynamics*, Mashinostroenie, Moscow, 1979.

[2] Bazarov, V., and Yang, V., "Liquid-Propellant Rocket Engine Injector Dynamics," *Journal of Propulsion and Power*, Vol. 14, No. 5, 1998, pp. 797–806. doi:10.2514/2.5343

[3] Ismailov, M., "Modeling of Classical Swirl Injector Dynamics," Ph.D. Thesis, Purdue Univ., West Lafayette, IN, 2010.

[4] Thomson, W., "Vibrations of a Columnar Vortex," *Proceedings of the Royal Society of Edinburgh*, Neill and Co., March 1880, pp. 155–168.

[5] Park, H., "Flow Characteristics of Viscous High-Speed Jets in Axial/Swirl Injectors," Ph.D. Thesis, Purdue Univ., West Lafayette, IN, 2005, Chap. 4.

[6] Richardson, R., "Linear and Nonlinear Dynamics of Swirl Injectors," Ph.D. Thesis, Purdue Univ., West Lafayette, IN, 2007.

[7] Richardson, R., Park, H., Canino, J., and Heister, S., "Nonlinear Dynamic Response Modeling of a Swirl Injector," 43rd AIAA/ASME/SAE/ASEE Joint Propulsion Conference and Exhibit, AIAA Paper 2007-5454, July 2007.

[8] Khil, T., Kim, S., Cho, S., and Yoon, Y., "Quantifying the Variation of Mass Flow Rate in a Simplex Swirl Injector by the Pressure Fluctuation for the Injector Dynamic Research," Asian Joint Conference on Propulsion and Power, Korea Inst. of Science and Technology Paper B1-1, Daejeon, Korea, March 2008.

[9] Khil, T., Kim, S., Cho, S., and Yoon, Y., "Quantifying the Variation of Mass Flow Rate Generated in a Simplex Swirl Injector by the Pressure Fluctuation," 44th AIAA/ASME/SAE/ASEE Joint Propulsion Conference and Exhibit, AIAA Paper 2008-4849, July 2008.

[10] Ahn, B., "Forced Excitation of Swirl Injectors Using a Hydro-Mechanical Pulsator," M.S. Thesis, Purdue Univ., West Lafayette, IN, 2009.

[11] Ahn, B., Ismailov, M., and Heister, S., "Forced Excitation of Swirl Injectors Using a Hydro-Mechanical Pulsator," 45th AIAA/ASME/SAE/ASEE Joint Propulsion Conference and Exhibit, AIAA Paper 2009-5043, Aug. 2009.

[12] Taylor, G., "The Mechanics of Swirl Atomizers," *7th International Congress on Applied Mechanics*, Vol. 2, Cambridge Univ., New York, 1948, pp. 280–285.

[13] Bayvel, I., and Orzechowski, Z., *Liquid Atomization*, Taylor and Francis, Philadelphia, 1993, Chap. 5-2.

[14] Chinn, J., "The Internal Flow Physics of Swirl Atomizer Nozzles," Ph.D. Thesis, Univ. of Manchester, Inst. of Science and Technology, Manchester, England, U.K., 1996.

[15] Darmofal, D., Khan, R., Greitzer, E., and Tan, C., "Vortex Core Behaviour in Confined and Unconfined Geometries: a Quasi-One-Dimensional Model," *Journal of Fluid Mechanics*, Vol. 449, 2001, pp. 61–84. doi:10.1017/S0022112001006103

[16] Spiegel, M., *Schaum's Outline of Mathematical Handbook of Formulas and Tables*, McGraw–Hill, New York, 2nd ed., 1968.

[17] Dean, R., and Dalrymple, R., *Water Wave Mechanics for Engineers and Scientists*, Prentice–Hall, Upper Saddle River, NJ, 1984.

[18] O'Hare, T., and Davies, A., "A New Model for Surface Wave Propagation Over Undulating Topography," *Coastal engineering*, Vol. 18, Nos. 3–4, 1992, pp. 251–266. doi:10.1016/0378-3839(92)90022-M

[19] Ismailov, M., and Heister, S., "Dynamic Response of Rocket Swirl Injectors, Part II: Nonlinear Dynamic Response," *Journal of Propulsion and Power*, Vol. 27, No. 2, 2011, pp. 412–421. doi:10.2514/1.B34045

[20] Miles, J., "Surface-Wave Scattering Matrix for a Shelf," *Journal of Fluid Mechanics*, Vol. 28, No. 4, 1967, pp. 755–767. doi:10.1017/S0022112067002423

E. Kim
Associate Editor